Stability and Rupture of an Ultrathin Ionic Wire

Bruno Focassio,[1,5] Tanna E. R. Fiuza,[2] Jefferson Bettini,[2] Gabriel R. Schleder,[2,1,3] Murillo H. M. Rodrigues,[4] João B. Souza Junior,[2] Edson R. Leite,[2,4,*] Adalberto Fazzio,[1,5] and Rodrigo B. Capaz[6,2,†]

[1]*Federal University of ABC (UFABC), 09210-580 Santo André, São Paulo, Brazil*
[2]*Brazilian Nanotechnology National Laboratory (LNNano), CNPEM, 13083-970 Campinas, São Paulo, Brazil*
[3]*John A. Paulson School of Engineering and Applied Sciences, Harvard University, Cambridge, Massachusetts 02138, USA*
[4]*Departamento de Química, Universidade Federal de São Carlos, 13565-905 São Carlos, São Paulo, Brazil*
[5]*Ilum School of Science, CNPEM, 13083-970 Campinas, São Paulo, Brazil*
[6]*Instituto de Física, Universidade Federal do Rio de Janeiro, 21941-909 Rio de Janeiro, Rio de Janeiro, Brazil*

Using a combination of *in situ* high-resolution transmission electron microscopy and density functional theory, we report the formation and rupture of ZrO_2 atomic ionic wires. Near rupture, under tensile stress, the system favors the spontaneous formation of oxygen vacancies, a critical step in the formation of the monatomic bridge. In this length scale, vacancies provide ductilelike behavior, an unexpected mechanical behavior for ionic systems. Our results add an ionic compound to the very selective list of materials that can form monatomic wires and they contribute to the fundamental understanding of the mechanical properties of ceramic materials at the nanoscale.

Monatomic wires (or chains) embody the ultimate realization of an ideal 1D system, providing a path to study the physics of atoms and electrons confined in a single dimension. The peculiar behavior of such extreme low-dimensional systems often reveals surprising and unexpected phenomena in their mechanical [1–3], magnetic [4], electronic transport [5,6], and vibrational properties [7,8]. Experimental realization of monatomic wires initially focused on metallic systems, particularly Au [1–3,5,6] and other $5d$ metals such as Ir and Pt [9]. Shortly after, covalent systems such as long carbon chains with alternating single and triple bonds (polyynes) have been stabilized inside carbon nanotubes [7,10], whereas shorter ones have been produced by pulling graphene until rupture [11,12].

In contrast to this early activity in metallic and covalent systems, to our knowledge, ionic wires have never been observed or produced experimentally down to the monatomic limit. Ionic systems are generally brittle and therefore considered to be less prone to form such ultrathin wires, in comparison to ductile metals. Moreover, local cation-anion charge balance in ionic systems is critical to their stability and it would be reasonable to imagine that keeping this balance during the whole process leading to monatomic wire formation would require an intricate and unlikely sequence of atomic rearrangements. In this Letter, we study monoclinic ZrO_2, a widely employed material for different applications, such as catalysts [13,14], composites for light-emitting diodes [15], water purification [16], Li-ion batteries [17], and biomedical applications [18].

In this Letter, using high-resolution transmission electron microscopy (HRTEM), we report the observation of highly stable ionic monatomic wires during the final stages of rupture between two nanoparticles of ZrO_2 under tensile stress. In support of experimental findings, *ab initio* molecular dynamics (AIMD) as well as quasistatic pulling simulations based on density functional theory (DFT) not only reproduce closely the observed atomic geometry of such wires, but also reveal an exquisite process of oxygen vacancy stabilization under stress that is key to provide the atomic-scale ductilelike behavior leading to ultrathin wire formation and rupture.

HRTEM is a powerful tool to follow atomic-scale dynamics in nanostructured materials. To visualize the dynamics of ZrO_2 atomic-wire formation, deformation, and rupture at room temperature using this technique, a novel preparation method was conceived. We prepare a freestanding ZrO_2 thin film from monoclinic ZrO_2 nanocrystals (m-ZrO_2 NCs) capped by organic ligands (oleic acid) via a dipping deposition process over a Cu grid covered by a holey carbon layer. The use of ZrO_2 NCs is essential to optimize the thickness of ZrO_2 thin film for HRTEM analysis, allowing for high-resolution images. After deposition, the m-ZrO_2 NC film was cleaned by electron beam illumination (e-beam shower) inside the TEM at high-vacuum operation conditions (10^{-7} torr), promoting efficient elimination of the organic capping layer and forming a freestanding layer of sintered nanoparticles (for more details, see the Supplemental Material [19]). The absence of a supporting membrane layer allows for unconstrained atomic mobility during the process. The inhomogeneous sintering process causes differential shrinkage, eventually leading to local tensile stress between
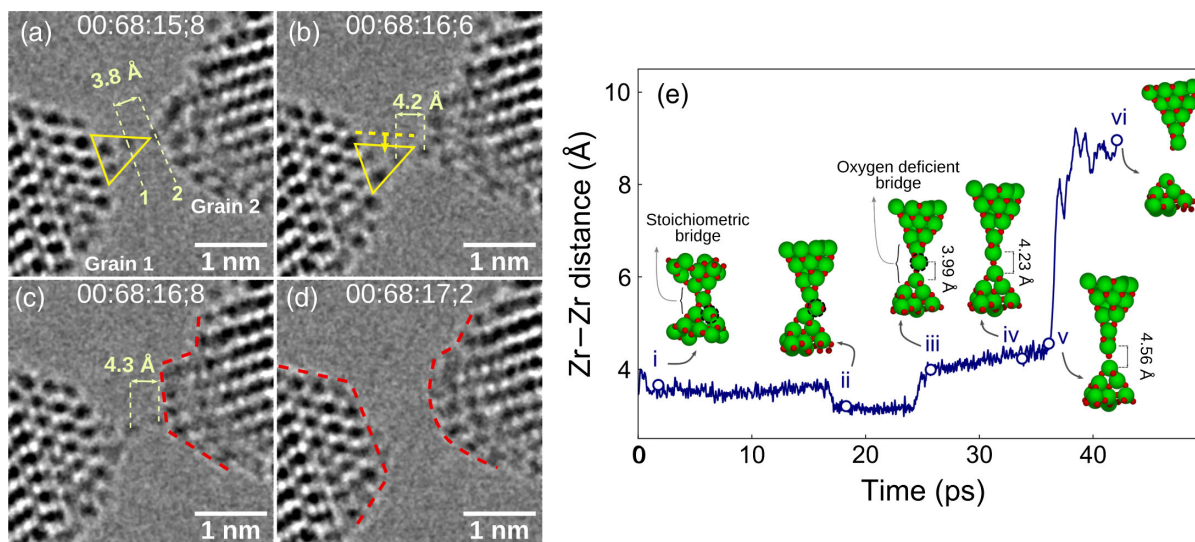
FIG. 1. HRTEM images of the ZrO_2 wire near rupture and Zr-Zr distance of m-ZrO_2 bipyramidal cluster calculated from AIMD simulations. Notice that only Zr atoms can be easily distinguished as dark spots in HRTEM images (oxygen atoms are invisible) [20]. (a) An atomic wire is seen with a Zr-O_2-Zr distance of 3.8 Å. (b) Complex atomic rearrangements take place, as suggested by the yellow triangle displacement indicated in the figure, leading to the formation of an oxygen vacancy at the atomic wire with an increased Zr-O-Zr distance of 4.2 Å, which evolves to 4.3 Å in (c), before rupture and (d) surface reconstruction. (e) Zr-Zr distance at the atomic wire calculated from AIMD simulations at room temperature vs simulation time. The insets show the structure of the m-ZrO_2 cluster at the indicated time frame. Inset (i) shows the initial setup after thermal equilibration at 300 K. As pulling simulation evolves, the Zr-Zr distance at the nanobridge remains roughly constant until (ii), when the atomic rearrangements leading to oxygen vacancy formation start to take place. At (iii), the oxygen-deficient atomic wire is formed, evolving with increasing tensile strain until Zr-O-Zr distances of approximately 4.56 Å, at (v), when rupture occurs.

a pair of sintered regions. This is the perfect condition to observe the stress-induced rupture between nanograins, whose final stages will lead to the formation of the ZrO_2 atomic wire. The cleaned freestanding ZrO_2 films were analyzed *in situ* using a Cs-corrected TEM microscope operating at 300 kV, thus allowing us to observe the formation and rupture of ZrO_2 ionic wires with unprecedented spatial and temporal resolution. It is important to mention that we did not observe extensive damage caused by the e-beam (for more details, see the Supplemental Material [19]).

Video M1 of the Supplemental Material shows a typical example of the dynamics of formation and rupture of the monatomic wire. Figure S1(a) shows a snapshot of this video, where we identify a precursor polycrystalline bridge from the cleaned ZrO_2 thin film. After several minutes under illumination, it gradually evolves to a bicrystal nanobridge, shown in Fig. S1(b). The bicrystal bridge continuously shrinks as a result of a complex combination of tensile stress and mass flux (details to be described elsewhere [20]) until it becomes a monatomic chain joining two grains [Figs. S1(c) and S1(d)]. Once again, to our knowledge this is the first observation of such atomic wires in brittle, ionic materials. Figure 1 shows in detail the HRTEM image sequence leading to the wire rupture. This sequence of images is interpreted with the help of two separate sets of *ab initio* calculations based on DFT: AIMD

pulling simulations at 300 K of a bipyramidal ZrO_2 cluster in Fig. 1(e) and quasistatic pulling simulations of two different model atomic chains (with and without an oxygen vacancy, as we shall explain) at 0 K in Fig. 2. Computational details can be found in the Supplemental Material [19], which also contains the full video (Video M2) of the AIMD simulations described in Fig. 1(e).

We analyze in parallel experiments and simulations. As shown in Fig. 1(a), in the initial steps of atomic-wire formation the experimental Zr-Zr atomic distance at the bridge is 3.8 Å, about 10% larger than the bulk value and consistent with our DFT-calculated value of 3.7 Å for a ZrO_2 stoichiometric monatomic wire under maximum tensile stress applied before rupture (Fig. 2). This is also consistent with the initial steps of our AIMD simulations [Fig. 1(e)], thus suggesting a Zr-O_2-Zr geometry as a precursor of the atomic wire. Then, suddenly, a series of complex atomic rearrangements are seen both in experiments [Figs. 1(b) and 1(c)] and in simulations, between insets (i) and (iii) in Fig. 1(e). As seen in the HRTEM images, following the displacement of a triangular cluster, highlighted by the yellow triangle in Figs. 1(a) and 1(b), the Zr-Zr atomic distance suddenly reaches 4.3 Å in Fig. 1(c), corresponding to an unexpected deformation of 25% in comparison with the bulk value. From the simulations, we conclude that the atomic rearrangements involve a complex combination of bond breakage and rotation, effectively
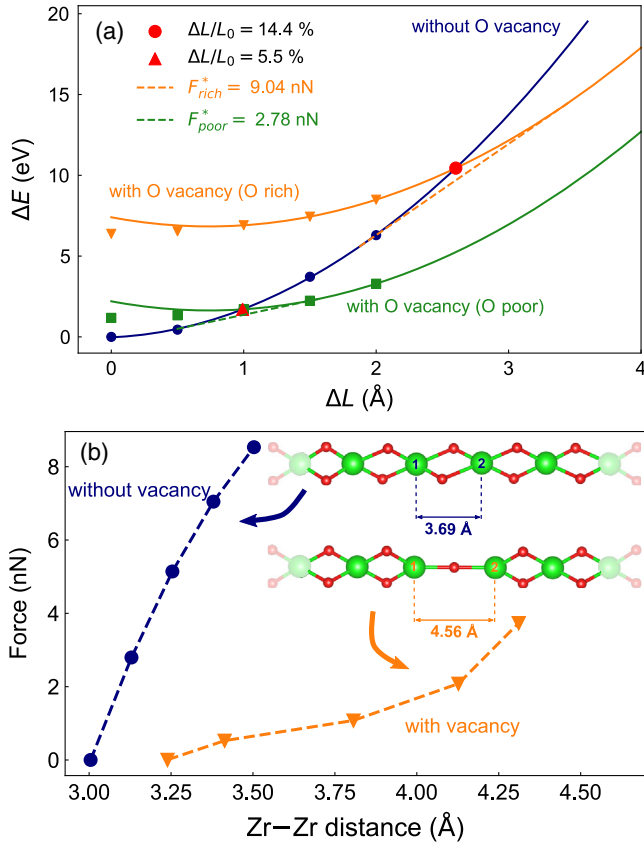
FIG. 2.   (a) DFT calculations showing the ZrO_2 wire energy (ΔE) vs unit cell length (with respect to equilibrium unit cell of the perfect wire) for the wire with (orange and green curves) and without (blue curves) an oxygen vacancy until complete rupture. The oxygen chemical potential is added to the total energy of the defective system in two extreme limits: O-rich (orange) and O-poor (green) conditions. The curves are parabolic fits to the last three DFT data points to improve the description of the rupture. The constant-length thermodynamic constraint is represented by the red circle and triangle for each chemical potential limit. The constant-force thermodynamic constraint is represented by the dashed lines in each chemical potential limit. (b) DFT calculations showing the ZrO_2 wire deformation curve for the stoichiometric and nonstoichiometric model until complete rupture. At each step, the shaded atoms (as shown in the insets) are fixed and the remaining atoms are allowed to relax. The force is taken on the fixed atoms at each ground-state geometry. The insets show the maximum Zr-Zr distance reached before the atomic-wire rupture. Rupture occurs after the last relaxation step (last point drawn). Comparing the two curves, we notice that the presence of an oxygen vacancy significantly decreases the force required to break the atomic wire and also allows for much longer wire extensions before rupture.

leading to the removal of an oxygen atom from the atomic bridge (i.e., creation of an oxygen vacancy) and establishing a Zr-O-Zr local stoichiometry, which in turn allows for the large Zr-Zr distances observed in HRTEM. Our static DFT calculations (Fig. 2, details in the Supplemental Material [19]) confirm this result, indicating that an

oxygen-deficient Zr-O-Zr motif can extend up to Zr-Zr distances of approximately 4.6 Å before rupture. Finally, Fig. 1(d) shows the system right after rupture, where one grain keeps well-oriented facets, while the other becomes rounded. Notice that the monatomic wire is observed in the HRTEM images for at least 1 s [as seen from the time counting between Figs. 1(a) and 1(c)], an extremely long time at the atomic scale, thus confirming that the observed structure is exceptionally stable.

Our AIMD simulations [Fig. 1(e)] suggest that rupture of the ZrO_2 wire is preceded by the spontaneous formation of an oxygen vacancy in the wire center. This is an intriguing result, since keeping the correct stoichiometry, both locally and globally, is usually an important requirement in ionic systems, where stability is closely intertwined with charge balance. We emphasize that our simulation cell has, from the start, the bulk ZrO_2 proportion, so oxygen depletion at the wire must be compensated by oxygen excess somewhere else in the simulation cell, i.e., a highly energetic vacancy-interstitial Frenkel-type defect must be created in the process. AIMD simulations for oxygen-depleted bridges are also performed and discussed in the Supplemental Material [19], and they do not change the qualitative picture described above.

It is interesting to understand the driving mechanism for this spontaneous defect formation process under tensile stress in more detail. To this end, we use as a starting point an ideal model of an infinite ZrO_2 wire [upper inset of Fig. 2(b)]. Detailed geometrical and dynamical stability properties of this particular wire are provided in the Supplemental Material. Figure 2(a) shows the total energy as a function of supercell length—measured with respect to the equilibrium length of the ideal stoichiometric wire—for both pristine and defective wires. In the case of defective wires, we add to the total energy curves the oxygen chemical potential in two extreme conditions: (i) the O-rich condition (orange curve), where $\mu_O = 1/2 E_{O_2}$ (where E_{O_2} is the total energy of an O_2 molecule), and (ii) the O-poor condition (green curve), $\mu_O = 1/2 E_{O_2} + 1/2 \Delta E^f_{ZrO_2}$ (where $\Delta E^f_{ZrO_2}$ is the formation energy of monoclinic ZrO_2) [21]. It is assumed that the oxygen chemical potential may vary continuously between these two limits and, as a consequence, there is a continuum of possible intermediate curves between the orange and green parabolas of Fig. 2(a).

Borrowing from the knowledge of 3D solids, in which the relative structural stability between two systems can be either analyzed at constant-volume or constant-pressure conditions, we use the equivalent concepts for these 1D systems by analyzing their relative stability at constant supercell length L or constant force F. For constant length, the relative stability is simply given by the total energy minimization. In other words, the crossing of total energy curves [indicated by the red circle and triangle in Fig. 2(a)]

TABLE I. Bond length variation for different theoretical conditions for the m-ZrO$_2$ nanowire geometric transition toward rupture and comparison with experimental bond lengths. μ_O is the oxygen chemical potential. The O-rich conditions stand for $\mu_O = 1/2E_{O_2}$ and the O-poor conditions stand for $\mu_O = 1/2E_{O_2} + 1/2\Delta E^f_{ZrO_2}$, with E_{O_2} the total energy of the O$_2$ molecule and $\Delta E^f_{ZrO_2}$ the formation energy of m-ZrO$_2$. The best match between theory and experiment occurs for O-rich and constant-length conditions.

μ_O condition	Constraint	Bond length variation (Å)
O-rich	Length	$3.66 \rightarrow 4.53$
	Force	$3.51 \rightarrow 5.42$
O-poor	Length	$3.25 \rightarrow 3.91$
	Force	$3.14 \rightarrow 4.18$
Experiment		$3.80 \rightarrow 4.20$

will correspond to the critical lengths beyond which the defective systems will have lower energy than the pristine system, leading to the spontaneous formation (i.e., negative formation energy) of an oxygen vacancy. As seen in Fig. 2(a), this critical strain is 14.4% for O-rich systems and 5.5% for O-poor systems. Such large strains are much larger than the yield strain of bulk ZrO$_2$ and they result primarily from the large variations in Zr-O-Zr bond angles under tensile stress, clearly a geometrical effect only possible for such a low-dimensional monatomic wire. Geometrical analysis of both structures at the crossing points leads to discontinuous jumps of Zr-Zr distances, from 3.25 to 3.91 Å in the O-poor condition and from 3.66 to 4.53 Å in the O-rich regime. These bond length discontinuities are measured experimentally to be from 3.8 to 4.2 Å [Figs. 1(a) and 1(b)].

For constant-force conditions, we search for the structure that minimizes the enthalpy $H = E - FL$. An equivalent geometrical formulation is given by the common tangent construction [dashed lines in Fig. 2(a)]. The common tangent slope gives the critical transition force (9.04 nN for O-rich and 2.78 nN for O-poor conditions). We can also calculate in this case the Zr—Zr bond length discontinuities (from 3.14 to 4.18 Å for O-poor and from 3.51 to 5.42 Å for O-rich conditions).

In Table I, we summarize these results for constant-length and constant-force conditions as a function of the oxygen chemical potential condition. Simply from the comparison between our calculated Zr-Zr distance discontinuities with experimental results, we could suggest that the final stages of our monatomic wire evolution occur in O-rich conditions at quasistatic (nearly constant) bridge length rather than constant force.

It is also instructive to analyze the force vs Zr-Zr distance for both pristine and defective ZrO$_2$ atomic wires, shown in Fig. 2(b). Because of its higher elastic constant, the force curve is much steeper for the pristine wire compared to the

defective one. This observation provides yet another way to interpret the spontaneous vacancy creation mechanism depicted in Fig. 2(a). As pulling progresses, eventually the energy cost of creating an oxygen vacancy will be lower than the elastic energy difference between the two stretched atomic wires and the oxygen vacancy will form spontaneously. Therefore, vacancy formation at the final stages of rupture can be seen as a mechanism for stress relief, leading to rupture at much lower forces than what would be expected for stoichiometric wires, as shown in Fig. 2(b).

The role of oxygen vacancies in the final stages of ZrO$_2$ monatomic wires formation and rupture can also be verified by performing the breaking experiments at low temperatures, using a cryoholder with liquid N$_2$ (77 K). As shown in the Supplemental Material [19], rupture still occurs at such low temperatures, in which we should expect significantly less atomic mobility. However, we observe in this case that the largest Zr-Zr distance before rupture is considerably smaller (3.6 Å) compared to the room-temperature value of 4.3 Å, as shown in Fig. S2. This smaller value is consistent with our quasistatic rupture simulations without oxygen vacancies [Fig. 2(b)]. Therefore, we propose that at low temperatures rupture takes place without the formation of oxygen vacancies, as a consequence of the kinetic hindrance of vacancy formation due to the lower atomic mobility.

In conclusion, we observed by HRTEM the formation, stability, and rupture of an ionic atomic wire under tensile stress. Our results add ZrO$_2$ to a very selective list of systems where the formation of such atomic wires has been observed, which previously included only 5d metals and carbon. *Ab initio* theory provides state-of-the-art identification of the detailed mechanisms for monatomic wire formation near rupture, which include the unexpected spontaneous formation of an oxygen vacancy under stress at room temperature. The oxygen vacancy provides extra elongation, softness, and irreversible (plastic) deformation to the monatomic wire, a behavior analogous to ductility in solids, albeit at the atomic scale. The results presented here are a step forward to a better understanding of the mechanical properties of ionic ceramic materials at the nanoscale. In particular, they contribute to understanding the structural behavior at the atomic scale of this class of materials, which may pave the way to future explorations and applications of mechanical properties of these systems.

*edson.leite@lnnano.cnpem.br
†capaz@if.ufrj.br

[1] A. I. Yanson, G. R. Bollinger, H. E. van den Brom, N. Agraït, and J. M. van Ruitenbeek, Formation and manipulation of a metallic wire of single gold atoms, Nature (London) **395**, 783 (1998).

[2] G. Rubio-Bollinger, S. R. Bahn, N. Agraït, K. W. Jacobsen, and S. Vieira, Mechanical Properties and Formation Mechanisms of a Wire of Single Gold Atoms, Phys. Rev. Lett. **87**, 026101 (2001).

[3] E. Z. da Silva, A. J. R. da Silva, and A. Fazzio, How Do Gold Nanowires Break?, Phys. Rev. Lett. **87**, 256102 (2001).

[4] D. Spišák and J. Hafner, Magnetism of ultrathin wires suspended in free space and adsorbed on vicinal surfaces, Phys. Rev. B **67**, 214416 (2003).

[5] H. Ohnishi, Y. Kondo, and K. Takayanagi, Quantized conductance through individual rows of suspended gold atoms, Nature (London) **395**, 780 (1998).

[6] V. Rodrigues, T. Fuhrer, and D. Ugarte, Signature of Atomic Structure in the Quantum Conductance of Gold Nanowires, Phys. Rev. Lett. **85**, 4124 (2000).

[7] X. Zhao, Y. Ando, Y. Liu, M. Jinno, and T. Suzuki, Carbon Nanowire Made of a Long Linear Carbon Chain Inserted inside a Multiwalled Carbon Nanotube, Phys. Rev. Lett. **90**, 187401 (2003).

[8] C. Fantini, E. Cruz, A. Jorio, M. Terrones, H. Terrones, G. Van Lier, J.-C. Charlier, M. S. Dresselhaus, R. Saito, Y. A. Kim, T. Hayashi, H. Muramatsu, M. Endo, and M. A. Pimenta, Resonance Raman study of linear carbon chains formed by the heat treatment of double-wall carbon nanotubes, Phys. Rev. B **73**, 193408 (2006).

[9] R. H. M. Smit, C. Untiedt, A. I. Yanson, and J. M. van Ruitenbeek, Common Origin for Surface Reconstruction and the Formation of Chains of Metal Atoms, Phys. Rev. Lett. **87**, 266102 (2001).

[10] L. Shi, P. Rohringer, K. Suenaga, Y. Niimi, J. Kotakoski, J. C. Meyer, H. Peterlik, M. Wanko, S. Cahangirov, A. Rubio, Z. J. Lapin, L. Novotny, P. Ayala, and T. Pichler, Confined linear carbon chains as a route to bulk carbyne, Nat. Mater. **15**, 634 (2016).

[11] C. Jin, H. Lan, L. Peng, K. Suenaga, and S. Iijima, Deriving Carbon Atomic Chains from Graphene, Phys. Rev. Lett. **102**, 205501 (2009).

[12] E. Hobi, R. B. Pontes, A. Fazzio, and A. J. R. da Silva, Formation of atomic carbon chains from graphene nanoribbons, Phys. Rev. B **81**, 201406(R) (2010).

[13] C. Zhou, J. Shi, W. Zhou, K. Cheng, Q. Zhang, J. Kang, and Y. Wang, Highly active ZnO-ZrO₂ aerogels integrated with H-ZSM-5 for aromatics synthesis from carbon dioxide, ACS Catal. **10**, 302 (2020).

[14] N. H. M. Dostagir, R. Rattanawan, M. Gao, J. Ota, J.-y. Hasegawa, K. Asakura, A. Fukouka, and A. Shrotri, Co single atoms in ZrO₂ with inherent oxygen vacancies for selective hydrogenation of CO₂ to CO, ACS Catal. **11**, 9450 (2021).

[15] Y. Duan, C. Ezquerro, E. Serrano, E. Lalinde, J. García-Martínez, J. R. Berenguer, and R. D. Costa, Meeting high stability and efficiency in hybrid light-emitting diodes based on SiO₂/ZrO₂ coated CsPbBr₃ perovskite nanocrystals, Adv. Funct. Mater. **30**, 2005401 (2020).

[16] Y. Chen, G. Yang, B. Liu, H. Kong, Z. Xiong, L. Guo, and G. Wei, Biomineralization of ZrO₂ nanoparticles on graphene oxide-supported peptide/cellulose binary nanofibrous membranes for high-performance removal of fluoride ions, Chem. Eng. J. **430**, 132721 (2022).

[17] M. Khalili Azar, M. A. Razmjoo Khollari, M. Esmaeili, E. Heidari, S. M. Hosseini-Hosseinabad, R. Siavash Moakhar, A. Dolati, and S. Ramakrishna, Enhanced electrochemical performance and thermal stability of ZrO₂- and rGO–ZrO₂-coated Li[Ni₀.₈Co₀.₁Mn₀.₁]O₂ cathode material for Li-ion batteries, ACS Appl. Energy Mater. **4**, 934 (2021).

[18] K. Srigurunathan, R. Meenambal, A. Guleria, D. Kumar, J. M. d. F. Ferreira, and S. Kannan, Unveiling the effects of rare-earth substitutions on the structure, mechanical, optical, and imaging features of ZrO₂ for biomedical applications, ACS Biomater. Sci. Eng. **5**, 1725 (2019).

[19] See Supplemental Material at http://link.aps.org/supplemental/10.1103/PhysRevLett.129.046101 for experimental details [20,22–24], experimental results at low temperatures [25], e-beam damage analysis [25–34], computational details on pulling and atomic-wire density functional theory simulations [35–45], AIMD simulations for oxygen-depleted bridges, and Videos M1–M3.

[20] T. E. R. Fiuza, B. Focassio, J. Bettini, G. R. Schleder, M. H. M. Rodrigues, J. B. Souza Junior, E. R. Leite, A. Fazzio, and R. B. Capaz, Atomic-scale description of tensile-induced desintering in nanostructured ceramics at room temperature. (unpublished).

[21] J. X. Zheng, G. Ceder, T. Maxisch, W. K. Chim, and W. K. Choi, First-principles study of native point defects in hafnia and zirconia, Phys. Rev. B **75**, 104112 (2007).

[22] C. J. Dalmaschio, E. G. da Silveira Firmiano, A. N. Pinheiro, D. G. Sobrinho, A. Farias de Moura, and E. R. Leite, Nanocrystals self-assembled in superlattices directed by the solvent–organic capping interaction, Nanoscale **5**, 5602 (2013).

[23] T. H. Lim, D. McCarthy, S. C. Hendy, K. J. Stevens, S. A. Brown, and R. D. Tilley, Real-time TEM and kinetic monte carlo studies of the coalescence of decahedral gold nanoparticles, ACS Nano **3**, 3809 (2009).

[24] M. A. van Huis, L. T. Kunneman, K. Overgaag, Q. Xu, G. Pandraud, H. W. Zandbergen, and D. Vanmaekelbergh, Low-temperature nanocrystal unification through rotations and relaxations probed by in situ transmission electron microscopy, Nano Lett. **8**, 3959 (2008).

[25] R. Egerton, P. Li, and M. Malac, Radiation damage in the TEM and SEM, Micron **35**, 399 (2004).

[26] N. Jiang, Electron beam damage in oxides: A review, Rep. Prog. Phys. **79**, 016501 (2016).

[27] W. Yuan, D. Zhang, Y. Ou, K. Fang, B. Zhu, H. Yang, T. W. Hansen, J. B. Wagner, Z. Zhang, Y. Gao, and Y. Wang, Direct in situ TEM visualization and insight into the facet-dependent sintering behaviors of gold on TiO₂, Angew. Chem., Int. Ed. **57**, 16827 (2018).

[28] T. Akita, M. Okumura, K. Tanaka, M. Kohyama, and M. Haruta, Analytical TEM observation of au nano-particles on cerium oxide, Catal. Today **117**, 62 (2006).

[29] R. L. Grosso, K. Vikrant, L. Feng, E. N. Muccillo, D. N. Muche, G. S. Jawaharram, C. M. Barr, A. M. Monterrosa, R. H. Castro, R. E. García, K. Hattar, and S. J. Dillon, Ultrahigh temperature *in situ* transmission electron microscopy based bicrystal coble creep in zirconia II: Interfacial thermodynamics and transport mechanisms, Acta Mater. **200,** 1008 (2020).

[30] J.-M. Costantini and F. Beuneu, Threshold displacement energy in yttria-stabilized zirconia, Phys. Status Solidi C **4,** 1258 (2007).

[31] E. Zarkadoula, R. Devanathan, W. J. Weber, M. A. Seaton, I. T. Todorov, K. Nordlund, M. T. Dove, and K. Trachenko, High-energy radiation damage in zirconia: Modeling results, J. Appl. Phys. **115,** 083507 (2014).

[32] F. K. McTaggart, Reduction of zirconium and hafnium oxides, Nature (London) **191,** 1192 (1961).

[33] J. Liu, A. H. Mir, G. He, M. Danaie, J. Hinks, S. Donnelly, H. Nordin, S. Lozano-Perez, and C. R. Grovenor, In-situ TEM study of irradiation-induced damage mechanisms in monoclinic-ZrO_2, Acta Mater. **199,** 429 (2020).

[34] Z. W. Wang and R. E. Palmer, Mass spectrometry and dynamics of gold adatoms observed on the surface of size-selected au nanoclusters, Nano Lett. **12,** 91 (2012).

[35] P. Hohenberg and W. Kohn, Inhomogeneous electron gas, Phys. Rev. **136,** B864 (1964).

[36] W. Kohn and L. J. Sham, Self-consistent equations including exchange and correlation effects, Phys. Rev. **140,** A1133 (1965).

[37] G. Kresse and J. Furthmüller, Efficiency of *ab-initio* total energy calculations for metals and semiconductors using a plane-wave basis set, Comput. Mater. Sci. **6,** 15 (1996).

[38] G. Kresse and J. Furthmüller, Efficient iterative schemes for *ab initio* total-energy calculations using a plane-wave basis set, Phys. Rev. B **54,** 11169 (1996).

[39] J. P. Perdew, J. A. Chevary, S. H. Vosko, K. A. Jackson, M. R. Pederson, D. J. Singh, and C. Fiolhais, Atoms, molecules, solids, and surfaces: Applications of the generalized gradient approximation for exchange and correlation, Phys. Rev. B **46,** 6671 (1992).

[40] J. P. Perdew, K. Burke, and M. Ernzerhof, Generalized Gradient Approximation Made Simple, Phys. Rev. Lett. **77,** 3865 (1996).

[41] G. Kresse and D. Joubert, From ultrasoft pseudopotentials to the projector augmented-wave method, Phys. Rev. B **59,** 1758 (1999).

[42] W. G. Hoover, Canonical dynamics: Equilibrium phase-space distributions, Phys. Rev. A **31,** 1695 (1985).

[43] S. Nosé, A unified formulation of the constant temperature molecular dynamics methods, J. Chem. Phys. **81,** 511 (1984).

[44] S. Nosé, A molecular dynamics method for simulations in the canonical ensemble, Mol. Phys. **100,** 191 (2002).

[45] W. Piskorz, J. Gryboś, F. Zasada, S. Cristol, J.-F. Paul, A. Adamski, and Z. Sojka, Periodic DFT and atomistic thermodynamic modeling of the surface hydration equilibria and morphology of monoclinic ZrO_2 nanocrystals, J. Phys. Chem. C **115,** 24274 (2011).